Journal of Materials Chemistry C

ROYAL SOCIETY OF CHEMISTRY

PAPER

View Article Online
View Journal | View Issue

Cite this: J. Mater. Chem. C, 2024, 12, 16741

Highly efficient and thermally stable broadband green-emitting $BaY_2Sc_2Al_2SiO_{12}:Ce^{3+}$ phosphors enabling warm-white LEDs with high luminous efficacy and high color rendering index

Xiaoyuan Chen and Xiaoyong Huang *

Exploring high-efficiency broadband green phosphors that match the eye's natural perception to produce light-emitting diodes (LEDs) with vivid color reproduction and exceptional saturated colors is highly desired. Herein, bright green luminescence is revealed in an all-inorganic single-phase Ce^{3+}-activated broadband garnet-type $BaY_2Sc_2Al_2SiO_{12}$ (BYSASO:Ce^{3+}) phosphor. Under 439 nm InGaN-based blue LED chip irradiation, the representative BYSASO:3%Ce^{3+} sample shows a suitable green emission with the maximum emission peak position located at 532 nm and an impressive full width at half-maximum (FWHM) of 125 nm, which can cover more cyan gap without sacrificing the green components. High internal quantum efficiency (IQE = 80.1%), outstanding thermal resistance behavior (73.9%@423 K) and color stability, and appropriate CIE color coordinates of (0.3700, 0.5394) make this excellent optical material suitable for industrial application. Finally, a prototype warm white LED device is obtained with the proposed green-emitting BYSASO:3%Ce^{3+} phosphor and a commercial red-emitting $(Ca,Sr)AlSiN_3:Eu^{2+}$ phosphor upon blue chip excitation, exhibiting extraordinary optical properties with a satisfactory R_a of 93.3 and comfortable CCT of 3958 K, as well as an excellent luminous efficacy of 105.3 lm W^{-1}. The results indicate that the green-emitting BYSASO:Ce^{3+} garnet phosphor has remarkable potential to serve as a conversion material for high-quality illumination.

Received 9th July 2024,
Accepted 5th September 2024

DOI: 10.1039/d4tc02906b

rsc.li/materials-c

1. Introduction

The rapid development of industrialization and urbanization is accompanied with the growth of human demands for energy and resources, and therefore, energy conservation and emission reduction are among the low-carbon sustainable development goals that the whole human society has been continuously pursuing.[1–9] Fortunately, phosphor-converted white light-emitting diodes (pc-WLEDs), the latest generation of solid-state lighting technology, are rapidly becoming an accessible and affordable way to dramatically improve energy savings because of their desirable optical characteristics, including exceptional efficiency, long operational lifetime, low power consumption, and environmentally benign components.[10–13] Presently, the most straightforward and best-selling approach for broad-spectrum white light production is to integrate a blue InGaN LED chip with a commercially available $Y_3Al_5O_{12}:Ce^{3+}$ (YAG:Ce^{3+}) phosphor emitting in yellow regions of the visible spectrum.[14] Unfortunately, the white light achieved with this scheme delivers an unsatisfactory color rendering index (CRI, $R_a < 90$) and a highly correlated color temperature (CCT > 4500 K) due to the faint cyan and red emissions in the visible region,[11,15–17] which are not suitable for its application in some special occasions with strict color requirements, such as museums, photography, galleries, and display industries. In this regard, two alternative strategies for generating white light while maintaining the color quality required for general illumination have been proposed. One is to employ blue LED chips coated with green and red phosphors. An alternative strategy involves coupling ultraviolet (UV) or near-UV LEDs with tri-color (red/green/blue) phosphors.[18–22] Surprisingly, both of the above schemes are effective in providing red emission components to improve the CRI index of LED lighting devices, but regrettably, the low light-conversion efficiency of the near-UV chip utilized in the latter and the presence of fluorescence reabsorption between multiple phosphor materials have severely hindered its widespread commercial applications.[23] Meanwhile, the "cyan cavity" between blue and green emission in the 480–520 nm region still exists, although not significantly, making it extremely challenging to achieve ultra-high-CRI warm white light for full-spectrum warm white LED lighting.[24–26] Considering that human vision is extremely sensitive to the green spectral region of visible light, high-quality green optical materials play an exceptionally

College of Physics and Optoelectronics, Taiyuan University of Technology, Taiyuan 030024, P. R. China. E-mail: huangxy04@126.com

important role in building human-centered solid-state lighting. Hence, exploring high-performance blue-light-excitable green-emitting phosphors that can provide both green and cyan emission components is a pressing need for enhancing the color vividness and saturation of warm-white LED devices toward high-quality healthy lighting.

Currently, commercially available green-emitting phosphors mainly include β-SiAlON:Eu^{2+}, $(Ba,Sr)_2SiO_4$:Eu^{2+}, $Y_3(Al,Ga)_5O_{12}$:Ce^{3+} and $Lu_3Al_5O_{12}$:Ce^{3+}. However, the above phosphors still suffer from several intrinsic defects in practical application. For instance, harsh preparation conditions (high temperature and pressure), the inability to be excited by blue chips with high photoelectric conversion efficiencies, and narrow-band emission that does not effectively cover the cyan region of β-SiAlON:Eu^{2+} remain a challenge for large-scale promotion.[27] Additionally, the disadvantages of the poor thermal resistance exist in $(Ba,Sr)_2SiO_4$:Eu^{2+} and $Y_3(Al,Ga)_5O_{12}$:Ce^{3+} phosphors.[28] Although $Lu_3Al_5O_{12}$:Ce^{3+} is a dominant green phosphor in the commercial market due to its broadband emission, the expensive raw materials (Lu_2O_3) required for synthesis and the limited FWHM value that does not cover more cyan emission are serious considerations for building warm white LED devices with a high color rendering index in general-purpose illumination applications. Accordingly, the exploration of a broadband oxide-based green-emitting phosphor capable of covering more cyan components that can be efficiently excited by blue LED chips is necessary.

Among the various oxide-based phosphors, Ce^{3+}-activated garnet-type phosphors have been favored by a wide range of research enthusiasts, of which, YAG:Ce^{3+} yellow powders, have been screened for the construction of warm-white LEDs.[23,29] This is because Ce^{3+} ions with characteristic spin-allowed 4f–5d transitions are introduced into the rigid structure with variable components having dodecahedral (eight-coordination), octahedral (six-coordination), or tetrahedral (four-coordination) arrangements, which can show different color-tunable emissions from blue to red under the influence of the surrounding crystal field environment.[30] Accordingly, the doping of Ce^{3+} into oxide-based garnet structures is a well-suitable option for the fabrication of high-performance green phosphors. Examples include $BaY_2Al_2Ga_2SiO_{12}$:Ce^{3+} (FWHM = 102 nm),[31] $Ca_2LaHf_2Al_3O_{12}$:Ce^{3+} (FWHM = 116 nm),[32] $CaY_2ZrScAl_3O_{12}$:Ce^{3+} (FWHM = 113 nm),[33] and $Lu_3Al_5O_{12}$:Ce^{3+} (FWHM = 97 nm),[34] but the values of FWHM are still limited (usually less than 120 nm) and they are somewhat incapable of capturing more of the cyan fluorescence component. Consequently, it is challenging to synthesize high-performance green-luminescent materials with FWHM of more than 120 nm through the rational screening of structurally variable garnet components.

Herein, we report the synthesis of an efficient broadband green-emitting BYSASO:Ce^{3+} optical material *via* the conventional high-temperature solid-phase reaction. The garnet-type structure and the occupancy of individual atoms are determined by XRD refinement and the Ce^{3+} content is optimized. The examination of optical properties reveals an asymmetric broadband emission (FWHM = 125 nm) with a maximum emission at 532 nm under blue light excitation, accompanying the high quantum efficiency (IQE = 80.1%) and appropriate CIE color coordinates of (0.3700, 0.5394). The high-temperature photoluminescence measurements shows a drop in luminescence intensity from room temperature to 73.9% at 423 K. A blue-excited white LED device incorporating the green-emitting BYSASO:3%Ce^{3+} and the commercial red-emitting (Ca,Sr)$AlSiN_3$:Eu^{2+} phosphors is fabricated, which exhibits a superior CRI of 93.3 and a low correlated color temperature of 3958 K, along with an excellent luminous efficacy of 105.3 lm W^{-1}. These results indicate that the green-emitting BYSASO:Ce^{3+} garnet-type phosphor is a promising candidate for the application in high-performance warm white LEDs.

2. Experimental section

2.1 Materials preparation

Polycrystalline samples of $Ba(Y_{1-x}Ce_x)_2Sc_2Al_2SiO_{12}$ (named: BYSASO:$x$$Ce^{3+}$; x = 0.5%, 1%, 3%, 5%, 7%) were prepared by a high-temperature solid-state reaction method. The starting materials, $BaCO_3$ (Aldrich, 99.999%), Y_2O_3 (Aldrich, 99.99%), Al_2O_3 (Aldrich, 99.99%), Sc_2O_3 (Aldrich, 99.99%), SiO_2 (99.9%) and $Ce(NO_3)_3{\cdot}6H_2O$ (Aldrich, 99.95%), were weighed in the desired stoichiometry and thoroughly mixed using an agate mortar and pestle for 30 min with the addition of ethanol as a grinding medium. The raw materials of the mixture were then sintered in a corundum crucible in a muffle furnace at 1450 °C for 6 hours under a CO reducing atmosphere. After that, the samples were gradually cooled naturally to room temperature. Finally, the products were further processed for subsequent characterization and testing.

2.2 Characterizations

The phase purity and crystal structures of the as-prepared experimental samples, BYSASO host, and the representative BYSASO:3%Ce^{3+} sample were determined using a powder X-ray diffractometer (XRD) with a Cu target as the radiation source (λ = 1.5406 Å) operating at 200 mA and 40 kV. The Rietveld refinement of the XRD profiles and the visualization of the refined crystal structure were carried out using the Fullprof program and the VESTA software, respectively.[35,36] The morphology and elemental mapping of the optimal BYSASO: 3%Ce^{3+} sample was observed using scanning electron microscopy (SEM) on a Hitachi Regulus SU8230 microscope. The diffuse reflectance (DR) spectra were collected using an ultraviolet-visible spectrophotometer (UV-3600 Plus, Shimadzu, Japan). Room temperature excitation and emission spectra were taken on a spectrophotometer (FS5, Edinburgh, UK) equipped with a continuous 150 W xenon flash lamp as a steady-state excitation source. The internal and external quantum efficiencies were determined using the same spectrometer, with the $BaSO_4$ integrating sphere as a reference. Temperature-dependent emission spectra in the range of 303 K to 443 K were recorded with a high-temperature fluorescence controller (TAP-02) compatible with the spectrophotometer described

above. A white LED device was manufactured by covering the as-prepared BYSASO:3%Ce^{3+} green-emitting phosphor and the commercial (Ca,Sr)$AlSiN_3$:Eu^{2+} red-emitting phosphor (Shenzhen looking long technology Co., LTD) on a 445 nm blue LED chip (San'an Optoelectronics Co., Ltd) using silicone resin. The optoelectronic performance of the corresponding LED devices was examined using a 50 mm integrating sphere spectroradiometer system (OHSP-350 M) with driving currents of 20–300 mA.

3. Results and discussion

3.1 Crystal structure and phase analysis

The phase purity and structure of the as-prepared phosphors are investigated using X-ray diffraction (XRD) patterns and Rietveld profile refinements. The XRD patterns of the BYSASO host and BYSASO:3%Ce^{3+} are shown in Fig. 1a, along with 2θ angles recorded in the range of 10–80°. The diffraction peaks of the two samples match well with the standard card of $Y_3Sc_2Al_3O_{12}$ (PDF #01-079-1846) with a minor amount of secondary phase of Sc_2O_3, suggesting that the obtained products are isostructural with garnet compounds. Compared to the BYSASO host, the Bragg diffraction peak position after the introduction of Ce^{3+} ion shifts towards a lower scattering angle in the enlarged XRD peak patterns as shown on the right side of Fig. 1a, which is probably driven by the lattice expansion due to the substitution of the larger Ce^{3+} ion (radius = 1.143 Å, CN = 8) for the smaller Y^{3+} ion (radius =1.019 Å, CN = 8) based on Bragg's law.[37,38] To further strengthen the speculations above and obtain detailed crystal structure information, the Rietveld structure refinements of the BYSASO host and BYSASO:3%Ce^{3+} are taken based on the structural data of $Y_3Sc_2Al_3O_{12}$ and Sc_2O_3. As shown in Fig. 1b and c, all the data including the observed pattern, experimental pattern, and the Bragg reflection position are highly compatible, corresponding to the reliability R-factors with $\chi^2 = 3.39$, $R_{wp} = 7.69\%$, $R_p = 6.03\%$ for the BYSASO host and $\chi^2 = 3.14$, $R_{wp} = 7.24\%$, $R_p = 5.62\%$ for the representative BYSASO:3%Ce^{3+} sample. The weight fraction of the Sc_2O_3 impurity in the BYSASO host and the representative BYSASO:3%Ce^{3+} sample are evaluated as 4.6% and 3.7%, respectively. The detailed crystallographic parameters and atomic coordinates are given in Tables 1 and 2, respectively. The results indicate that BYSASO and BYSASO:3%Ce^{3+} compounds belong to the cubic garnet crystal system with the $Ia\bar{3}d$ space group, and the cell parameters are described as $a = b = c = 12.31653$ Å, $\alpha = \beta = \gamma = 90°$, and $V = 1868.378(0.029)$ Å^3 for the former and $a = b = c = 12.31961$ Å, $\alpha = \beta = \gamma = 90°$ and $V = 1869.780(0.034)$ Å^3 for the latter. The cell volume increases in the BYSASO:3%Ce^{3+} sample compared to the BYSASO host, indicating the successful substitution of Ce^{3+} for Y^{3+} ions within the host lattice.

Following the empirical principle, the acceptable percentage difference in ionic radius between the dopant ion and the substitution ion should be less than 30%, which can be written as follows:[39]

$$D_r = 100\% \times \left| \frac{R_m(CN) - R_d(CN)}{R_m(CN)} \right| \quad (1)$$

where CN is the coordination number, R_m(CN) and R_d(CN) are the radii of the substituted ions and dopant ions, respectively.

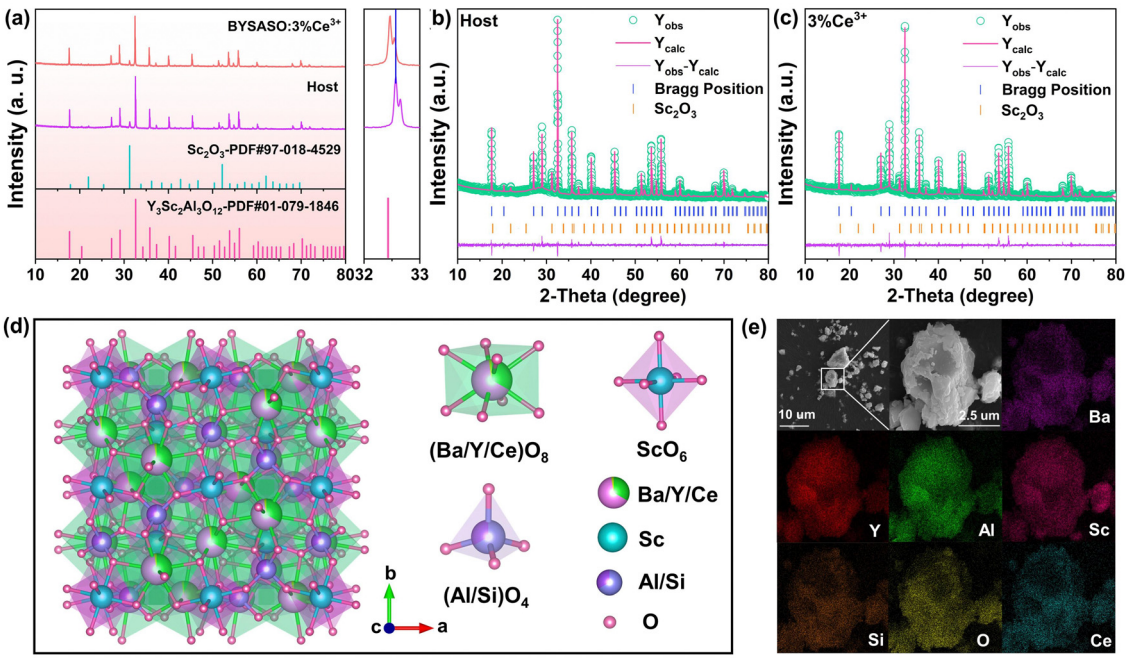

Fig. 1 (a) XRD patterns of the BYSASO host and the as-prepared BYSASO:3%Ce^{3+} sample. The Rietveld refinements of the BYSASO host (b) and the representative BYSASO:3%Ce^{3+} sample (c). (d) Crystal structure diagram of BYSASO:3%Ce^{3+} and the coordination environment of Ba, Y, Sc, Al, Si, O, Ce. (e) SEM patterns and elemental mapping of the optimal BYSASO:3%Ce^{3+} sample.

Table 1 The refined crystallographic parameters of the BYSASO host and BYSASO:3%Ce^{3+} samples

Compounds	BYSASO	BYSASO:3%Ce^{3+}
Crystal system	Cubic	Cubic
Space group	$Ia\bar{3}d$	$Ia\bar{3}d$
Lattice parameters	$a = b = c = 12.31653$ Å $\alpha = \beta = \gamma = 90^\circ$	$a = b = c = 12.31961$ Å $\alpha = \beta = \gamma = 90^\circ$
Unit cell volume	$V = 1868.378(0.029)$ Å^3	$V = 1869.780(0.034)$ Å^3
R_p	6.03%	5.62%
R_{wp}	7.69%	7.24%
χ^2	3.39	3.14

Table 2 Atomic coordinates of the BYSASO host and BYSASO:3%Ce^{3+} samples

Atom	Position	x	y	z	Occ.
BYSASO					
Ba	24c	0.12000	0.00000	0.25000	0.3333
Y	24c	0.12000	0.00000	0.25000	0.6667
Sc	16a	0.00000	0.00000	0.00000	1.0000
Al	24d	0.37500	0.00000	0.25000	0.6667
Si	24d	0.37500	0.00000	0.25000	0.3333
O	96h	0.03528	0.05350	0.65770	1.0000
BYSASO:3%Ce^{3+}					
Ba	24c	0.12000	0.00000	0.25000	0.3333
Y	24c	0.12000	0.00000	0.25000	0.6416
Ce	24c	0.12000	0.00000	0.25000	0.0251
Sc	16a	0.00000	0.00000	0.00000	1.0000
Al	24d	0.37500	0.00000	0.25000	0.6667
Si	24d	0.37500	0.00000	0.25000	0.3333
O	96h	0.03594	0.05281	0.65801	1.0000

Given the 12.2% mismatch ratio of Y^{3+} ions (1.019 Å, CN = 8) and Ce^{3+} ions (1.143 Å, CN = 8) with an identical charge, the formation of solid-solution $Ba(Y_{1-x}Ce_x)_2Sc_2Al_2SiO_{12}$ compounds by substituting eight-coordinated Y^{3+} lattice sites with Ce^{3+} is further confirmed in combination with the above ionic lattice occupation from XRD refinement. As is depicted in Fig. 1d, the proposed BYSASO:3%Ce^{3+} solid-solution compound has the cubic garnet structure in which $Ba^{2+}/Y^{3+}/Ce^{3+}$ ions occupy eight-coordinate dodecahedral sites, Sc^{3+} ions occupy six-coordinate octahedral sites, and Al^{3+}/Si^{4+} ions occupy four-coordinate tetrahedral sites. Different polyhedra are joined by sharing corners or edges to generate a three-dimensional rigid network structure. Fig. 1e presents the SEM image of BYSASO:3%Ce^{3+} phosphor particles and the corresponding energy dispersive spectrometer (EDS) elemental mapping results. SEM reveals a homogeneous irregular nubby morphology with crystal sizes ranging from a few microns to more than 10 microns. EDS results indicate that the elements Ba, Y, Sc, Al, Si, O, and Ce are evenly distributed over the whole particle surface.

3.2 Optical band gap and photoluminescence properties

Fig. 2a displays the DR spectrum of the BYSASO:3%Ce^{3+} phosphor. As presented, the two characteristic absorption peaks at around 350 nm and 440 nm are attributed to the two characteristic transitions from the 4f ground state to the 5d excited states of the Ce^{3+} ion. The optical bandgap values of BYSASO:3%Ce^{3+} sample can be roughly estimated with the following equation:[40]

$$F(R_\infty) = \frac{(1-R)^2}{2R} \quad (2)$$

$$[F(R_\infty)h\upsilon]^n = C(h\upsilon - E_g) \quad (3)$$

where $F(R_\infty)$ represents the absorption, R stands for the reflectance, $h\upsilon$ is the photon energy, C is the absorption constant, and E_g refers to the optical bandgap. Generally, the type of electronic transition determined by the value of n is a direct allowed transition in this garnet system ($n = 1/2$).[41] Thus, the optical bandgap of the BYSASO:3%Ce^{3+} sample is calculated as 4.50 eV. The wide bandgap indicates that BYSASO is a suitable host material for doping Ce^{3+} luminescence centers. It may also predict higher resistance to luminescence thermal quenching for BYSASO:3%Ce^{3+} phosphor, because a narrow bandgap commonly enhance the likelihood of luminescence quenching through thermally activated photoionization.[42]

Room-temperature photoluminescence excitation (PLE) and photoluminescence emission (PL) spectra of the representative BYSASO:3%Ce^{3+} sample are presented in Fig. 2b. Excitation spectra containing two characteristic peaks with wavelengths ranging from 200 nm to 500 nm are collected using λ_{em} = 532 nm, with the maximum peak of the high energy level positioned at 350 nm and another low energy level situated at 439 nm, which correspond to the Laporte-allowed electronic transitions of Ce^{3+} ions with two 4f ground state energy levels ($^2F_{7/2}$ and $^2F_{5/2}$) under spin–orbit coupling to 5d excited state energy levels, respectively.[43] This result is also consistent with the two strong absorption bands in the DR spectrum of Fig. 2a. The broadband absorption in the blue region indicates that the proposed phosphor can be effectively energized by commercial blue LED chips with high fluorescence conversion efficiency.[44] The PL spectrum recorded at 439 nm displays an asymmetric broadband emission extending from 460 nm to 800 nm, along with the strongest peak located at 532 nm and the FWHM value up to 125 nm. Impressively, this large FWHM value is greater than some of the currently reported Ce^{3+}-activated green emission phosphors, such as $Lu_2SrAl_4SiO_{12}:Ce^{3+}$ (105 nm),[45] $CaY_2ZrScAl_3O_{12}:Ce^{3+}$ (113 nm),[33] $Lu_3Al_5O_{12}:Ce^{3+}$ (97 nm),[34] $Ca_2YZr_2Al_3O_{12}:Ce^{3+}$ (98 nm),[46] and $BaY_2Al_2Ga_2SiO_{12}:Ce^{3+}$ (76 nm),[31] indicating that it is beneficial for realizing high-CRI white LEDs. This emission band is also capable of being decomposed into two Gaussian curves centered at 515 nm (19417 cm^{-1}) and 566 nm (17667 cm^{-1}), corresponding to the spin–orbit-assisted transitions from the lowest 5d excited state energy to the $^2F_{7/2}$ and $^2F_{5/2}$ ground state. The energy difference is evaluated as 1750 cm^{-1}, which approaches the theoretical value of 2000 cm^{-1}, identifying the activation center of Ce^{3+} as being within individual crystallographic sites.[47] Combined with the XRD refinement results of BYSASO:3%Ce^{3+}, it was confirmed that the luminescence band lying at 532 nm is derived

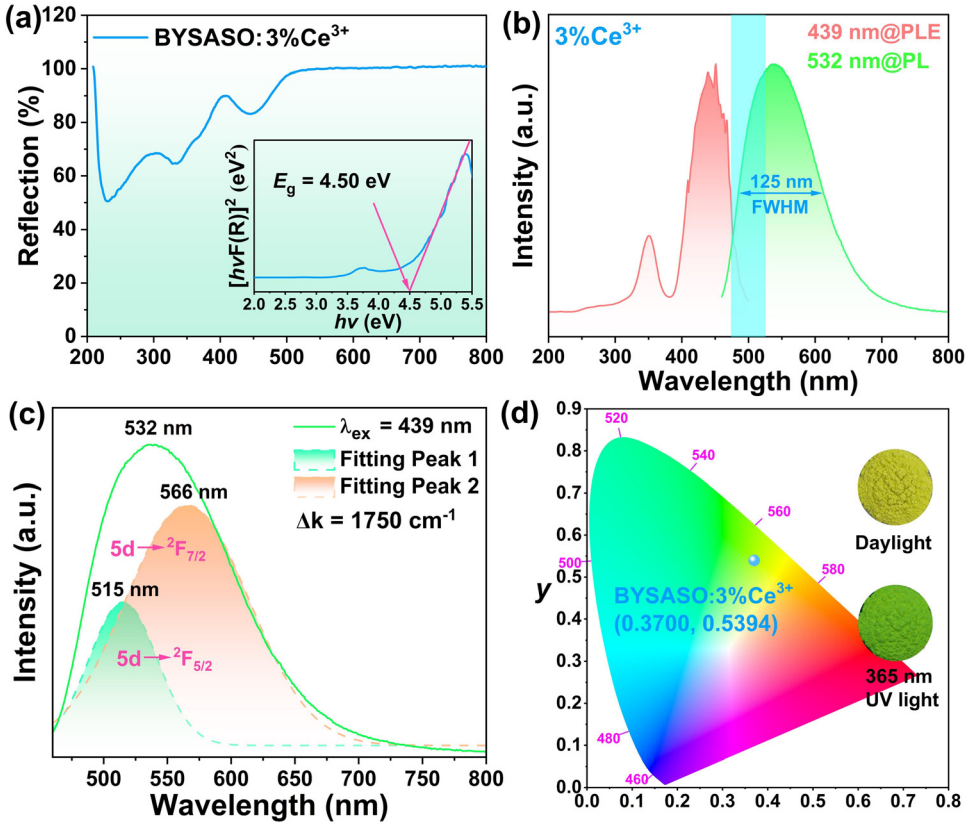

Fig. 2 (a) The DR spectrum and optical bandgap of BYSASO:3%Ce^{3+}. (b) PLE and PL spectra of BYSASO:3%Ce^{3+}. (c) Gaussian fitting curves of the PL spectrum for BYSASO:3%Ce^{3+}. (d) CIE color coordinates of the BYSASO:3%Ce^{3+} phosphor. The insets show the corresponding digital photographs under daylight and 365 nm near-UV lamp irradiation.

from Ce^{3+} sitting on the dodecahedron [YO_8] lattice site. The corresponding CIE chromaticity diagram of (0.3700, 0.5394) and digital photographs under a 365 nm near-UV illumination also highlight the bright green emission located in the green region. The currently available white LEDs in the market consisting of a yellow YAG:Ce^{3+} phosphor covered with blue InGaN LED chips have a significant gap in the cyan region at 480–520 nm, which somewhat weakens the quality and vividness of the colors presented by the object itself. Although a smooth and complete full-visible emission spectrum can be produced by integrating cyan phosphors into the above combination approach, the reabsorption effect and thermal degradation rates between different phosphors are still challenging issues that need to be solved. Accordingly, the as-prepared BYSASO:3%Ce^{3+} broadband green phosphor can cover more cyan emission (the cyan-colored shadow in Fig. 2b) while providing the adequate green emission component, making it a prospective candidate to bridge the cyan gap for constructing high-CRI white LEDs.

A series of BYSASO:$x$$Ce^{3+}$ (x = 1%, 3%, 5%, 7%, 9%) phosphors are systematically investigated to understand their concentration-dependent spectroscopic properties. Monitored at 532 nm, all PLE spectra in Fig. 3a exhibit two strong broadband absorptions in the near-UV (350 nm) and blue (439 nm) light regions, respectively. With a gradual increase in the amount of Ce^{3+} incorporated in the BYSASO host, the intensity of the excitation peaks initially increased and then decreased, reaching a maximum at 3%. Fig. 3b presents the variation of the luminescence intensity, showing concentration-dependent emission spectra in a consistent tendency toward co-excitation under the strongest excitation at 439 nm. The normalized PL spectra as a function of Ce^{3+} concentration are plotted in Fig. 3c. With increasing the Ce^{3+} concentration from 0.5% to 7%, the position of the maximum emission peak exhibits a significant red-shift ranging from 528 nm to 549 nm. When this red-shift is reflected in CIE coordinates changing from (0.3445, 0.5400) at 0.5% to (0.3975, 0.5322) at 7%, and the corresponding digital photographs under a 365 nm near-UV lamp shown in Fig. 3d, the emission color perceived by the human eye is linearly off-set from green to yellow-green, suggesting that the introduction of different concentrations of Ce^{3+} ions into the BYSASO host can achieve tunable color emission. The observed red-shift in the PL spectra can be elucidated by the strength of the crystal field splitting proposed by Dorenbos with the following equation:[48]

$$D_q = \frac{ze^2r^4}{6R^5} \quad (4)$$

where D_q denotes the magnitude of energy level separation, z refers to the charge or valence of the anion, e is the electron

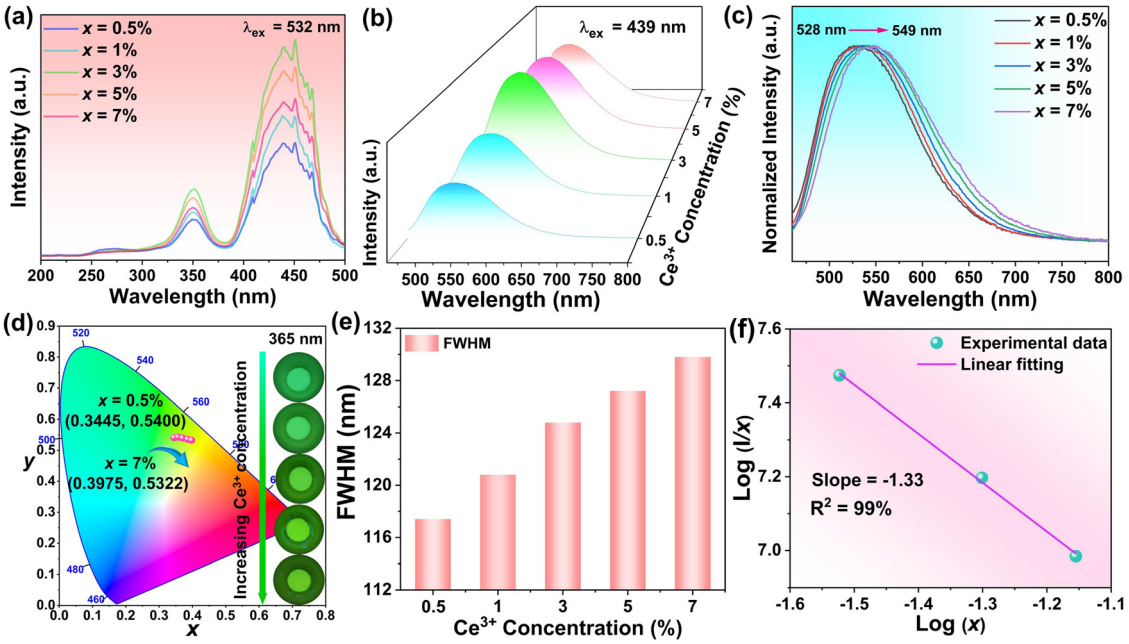

Fig. 3 Concentration-dependent PLE (a) and PL (b) spectra of the series of BYSASO:xCe^{3+} (x = 0.5%, 1%, 3%, 5% and 7%) phosphors. (c) The normalized PL spectra as a function of Ce^{3+} concentration upon 439 nm excitation. (d) CIE chromaticity diagram for phosphors as a function of Ce^{3+} concentration. The inset displays the corresponding digital photographs under 365 nm near-UV irradiation. (e) Concentration-dependent FWHM values. (f) Dependence of $\log\left(\frac{I}{x}\right)$ on log(x) in BYSASO:xCe^{3+} phosphors (x = 3%, 5% and 7%).

charge, r represents the radius of 5d wave functions, and R corresponds to the distance between the luminescence center ion and its ligand. D_q is inversely proportional to R^5. According to the above description, when the larger radius Ce^{3+} (r = 1.143 Å) ions are introduced into the BYSASO crystal lattice to replace the Y^{3+}ions with smaller radius (r = 1.019 Å), the dodecahedron [CeO$_8$] is severely compressed from the neighboring atoms in the rigid garnet structure, which results in a shortening of the Ce–O bond distance.[25,49] This induces an increase in crystal field splitting in the lowest 5d energy level orbitals of Ce^{3+} ions, which, in turn, contributes to a red-shift in the PL spectra.[50] The resonance energy transfer within the Ce^{3+} ions from the high-energy to the low-energy luminescence center is also responsible for the red-shifted emission, as can be observed from the partial overlap between the PLE and PL spectra on the high-energy side of the emission band in Fig. 2b. Meanwhile, the FWHM values of the emission bands modulated by the increase in the Ce^{3+} concentration demonstrate a non-negligible broadening from 117 nm to 130 nm in Fig. 3e, which probably stems from the enhanced electro–phonon coupling of the Ce^{3+} activator center with the vibrational modes of the BYSASO host lattice.[51,52]

As illustrated in Fig. 3a and b above, the concentration quenching phenomenon occurs when the substitution concentration of Ce^{3+} is more than 3% due to the non-radiative energy transfer between the two nearest activators.[53] Typically, the critical distance (R_c) is widely accepted for analyzing energy transfer processes, and can be evaluated by the following expression proposed by Blasse:[54]

$$R_c = 2\left(\frac{3V}{4\pi x_c N}\right)^{\frac{1}{3}} \quad (5)$$

where V stands for the unit cell volume of the crystallographic unit cell, x_c stands for the critical concentration of Ce^{3+}, and N refers to the number of lattice sites in the unit cell occupied by the rare-earth Ce^{3+} ions. In the optimal BYSASO Ce^{3+} sample, R_c is approximately evaluated as 25.60 in terms of V = 1869.780(0.034) Å^3, N = 8, and x_c = 3% following the results of the Rietveld refinement described above. This value is much larger than the critical distance (5 Å) at which exchange interactions occur. As a result, the electric multipolar interaction deduced from Dexter's theory may be the dominant concentration quenching mechanism, which can be distinguished by the following equation:[55]

$$\frac{I}{x} = K\left(1 + \beta(x)^{\frac{\theta}{3}}\right)^{-1} \quad (6)$$

where I represents the luminescence intensity, x stands for the activator ion concentration, K and β are the constants for a given host crystal, respectively, and θ is determined by the type of electric multipolar interactions, where θ = 6, 8, and 10 correspond to dipole–dipole, dipole–quadrupole, and quadrupole–quadrupole interactions, respectively. As illustrated in Fig. 3f, the relationship between log(I/x) and log(x) can be fitted linearly as −1.33 ($-3/\theta$), indicating that the mechanism of concentration quenching in the BYSASO:xCe^{3+} phosphor mainly involves dipole–dipole interactions. Radiative reabsorption is also a non-negligible factor in concentration quenching due to the partial overlap of the PL and PLE bands in Fig. 2b.[56]

One of the most valuable optical properties of a phosphor is photoluminescence quantum efficiency, which can be characterized by measuring the internal and external

quantum efficiency through the expression of the following formula:

$$\mathrm{IQE} = \frac{\int L_s}{\int E_R - \int E_s} \quad (7)$$

$$\varepsilon = \frac{\int E_R - \int E_s}{\int E_R} \quad (8)$$

$$\mathrm{EQE} = \mathrm{IQE} \times \varepsilon \quad (9)$$

where IQE is the internal quantum efficiency, which is the integral ratio between the photons absorbed and emitted by the luminescent centers with respect to $BaSO_4$ as a reference. ε represents the absorption efficiency. EQE refers to the external quantum efficiency, which is the integral ratio of photons emitted *versus* the total incident photons. L_s denotes the integral areas of the emission spectrum. E_R and E_s stand for the integral sphere of the scattering spectra of the tested sample and $BaSO_4$ as the reference, respectively. According to the experimental data, the optical parameters of the BYSASO:xCe^{3+} phosphors are summarized in Table 3, wherein, the IQE, AE and IQE of the proposed BYSASO:3%Ce^{3+} phosphor were evaluated as 80.1%, 61.6%, and 49.3%, respectively. The outstanding IQE value is superior to most other green phosphors previously reported, including $K_3La(Ca)(PO_4)_2$:Eu^{2+} (IQE = 55.25%),[24] $CaY_2ZrScAl_3O_{12}$:Ce^{3+} (IQE = 63.1%),[33] $Ca_2LaHf_2Al_3O_{12}$:Ce^{3+} (IQE = 46.5%),[32] $Ba_5La_3MgAl_3O_{15}$:Ce^{3+} (IQE = 27%),[57] and $Ca_2YHf_2Al_3O_{12}$:Ce^{3+} (IQE = 68.5%).[58]

3.3 Thermal stability

Typically, the weakening of fluorescence intensity due to increased probability of possible non-radiative electron transfer, enhanced electro–phonon coupling, and clustering of higher vibrational levels can limit phosphor applications to some extent.[59–61] The shift in the position of the emission peaks will also impact the chromaticity of the LED lamp, thus reducing its color purity. Accordingly, the additional evaluation of the optical properties of fluorescent materials with respect to temperature is required for practical lighting applications since LED lamps can operate at temperatures up to approximately 423 K. Fig. 4a illustrates the temperature-dependent emission spectra of the as-prepared BYSASO:3%Ce^{3+} phosphor taken at 20 K intervals from 303 K to 443 K, and the corresponding contour plot of the spectra is shown in Fig. 4b. The emission intensity of this phosphor exhibits a continuous decreasing trend with the gradual increase in temperature, which is due to thermal quenching. The calculation of the normalized integral intensity in Fig. 4c indicates that about 73.9% of the emission intensity can be maintained at 423 K compared to room temperature. BYSASO:3%Ce^{3+} features superior thermal robustness in comparison to most Ce^{3+}-activated green garnet-type phosphors reported in recent years, such as $Ca_2LaZr_2Ga_3O_{12}$:Ce^{3+} (48%@403 K),[62] $CaY_2ZrScAl_3O_{12}$:Ce^{3+} (55%@423 K),[33] $Ca_2YZr_2Al_3O_{12}$:Ce^{3+} (62.1%@423 K),[46] and $CaY_2HfGa(AlO_4)_3$:Ce^{3+} (46%@423 K).[63] Thermally-induced degradation of PL intensity may result from the enhancement of the probability of nonradiative relaxation pathways due to phonon–electron interactions in high-temperature environments.[64] In order to gain a more in-depth insight into the thermal effects on fluorescence intensity, it is necessary to understand the thermal quenching mechanism of phosphors. Generally, the dominant quenching pathway in rare-earth-substituted phosphors is thermal cross-relaxation, which can be characterized by the thermal activation energy, (E_a), derived by experimentally fitting temperature-dependent emission data to the Arrhenius equation:[65]

$$\frac{I_T}{I_0} = \left[1 + C\exp\left(-\frac{E_a}{k_B T}\right)\right]^{-1} \quad (10)$$

where I_T represents the emission intensity at a given temperature T, I_0 stands for the initial emission intensity, C refers to a constant, T is the operating temperature, and k refers to the Boltzmann constant of 8.62×10^{-5} eV K^{-1}. Thus, E_a, represented by the slope of the linear fitting in Fig. 4d, is identified as 0.26 eV. Typically, a larger thermal activation energy means that the nonradiative transition from the lowest 5d excited state energy level to the 4f ground state energy level of the electron is attenuated, resulting in superior thermal resistance, and *vice versa*.

Further analysis of the normalized emission spectra of the optimal BYSASO:3%Ce^{3+} sample in Fig. 4e indicates a negligible emission shift or change in the FWHM values as the temperature increased from 303 K to 443 K, suggesting exceptional color stability. The corresponding CIE color coordinates under different temperatures are calculated and the data are presented in Fig. 4f. With gradually rising temperatures, the CIE color coordinates demonstrate a slight shift moving from (0.3744, 0.5564) at 303 K to (0.3844, 0.5487) at 443 K. The associated chromaticity shift (ΔE) is evaluated in accordance with the following equation:[66]

$$\Delta E = \sqrt{\left(u'_f - u'_i\right)^2 + \left(v'_f - v'_i\right)^2 + \left(w'_f - w'_i\right)^2} \quad (11)$$

where $u' = 4x/(3 - 2x + 12y)$, $v' = 9y/(3 - 2x + 12y)$ and $w' = 1 - v' - u'$. u' and v' are chromaticity coordinates in the $u'v'$ uniform color space, x and y are chromaticity coordinates in the CIE1931 color space, and i and f represent the initial (303 K) and final temperatures (423 K), respectively. Depending on the available data from the relevant experiments, ΔE is quantitatively assessed as 8.09×10^{-3}, which is less than that of the commercial red phosphor of $CaAlSiN_3$:Eu^{2+} ($\Delta E = 4.4 \times 10^{-2}$ at 423 K),[67] and the commercial blue phosphor of $BaMgAl_{10}O_{17}$:Eu^{2+} ($\Delta E = 1.52 \times 10^{-2}$ at 423 K).[68] These results

Table 3 Luminescence properties of BYSASO:xCe^{3+} (x = 0.5%, 1%, 3%, 5%, 7%) phosphors under an excitation of 439 nm

x (%)	λ_{em} (nm)	FWHM (nm)	CIE (x, y)	IQE (%)	AE (%)	EQE (%)
0.5	528	117	(0.3445, 0.5400)	92.5	49.2	45.5
1	530	121	(0.3563, 0.5423)	88.7	52.7	46.7
3	532	125	(0.3700, 0.5394)	80.1	61.6	49.3
5	539	127	(0.3856, 0.5353)	72.4	67.4	48.8
7	549	130	(0.3975, 0.5322)	59.2	75.2	44.5

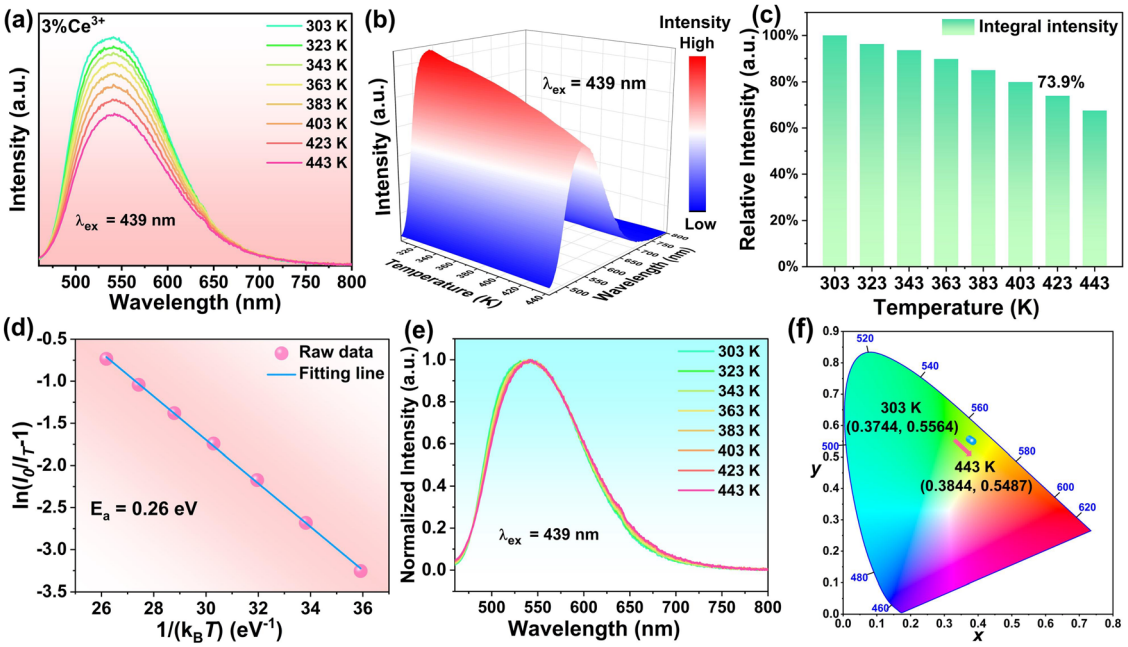

Fig. 4 (a) Temperature-dependent PL spectra of the as-fabricated BYSASO:3%Ce^{3+} sample. (b) The corresponding 3D contour plot of temperature dependence. (c) The variation trend of the relative integral emission intensity of the BYSASO:3%Ce^{3+} phosphor as a function of temperature. (d) The calculation of the thermal quenching activation energy for the BYSASO:3%Ce^{3+} sample. (e) Temperature-dependent normalized PL spectra of the BYSASO:3%Ce^{3+} sample. (f) CIE chromaticity diagram of the BYSASO:3%Ce^{3+} phosphor as a function of temperature.

indicate that the as-prepared broadband green-emitting BYSASO:3%Ce^{3+} garnet phosphor possesses remarkable color stability and is well-suited for integration into LED devices for general illumination and display.

3.4 White LED application

Inspired by the excellent luminescence efficiency and superior thermal stability, a white LED device is fabricated to investigate the potential of the green-emitting BYSASO:3%Ce^{3+} garnet phosphor in white lighting applications. Accordingly, a prototype LED device is constructed by integrating a 445 nm blue LED chip with a mixture of the as-synthesized green-emitting BYSASO:3%Ce^{3+} phosphor and the commercial red-emitting (Ca,Sr)$AlSiN_3$:Eu^{2+} phosphor. The resulting photoluminescence spectrum in Fig. 5a exhibits a bright white light with a satisfactory CRI value (R_a = 93.3), comfortable CCT of 3958 K, and an excellent luminous efficacy (LE) of 105.3 lm W^{-1} under a 20 mA forward-bias current. With the integration of the blue LED chip (0.1457, 0.0320), BYSASO:3%Ce^{3+} green phosphor (0.3700, 0.5394) and the commercial (Ca,Sr)$AlSiN_3$:Eu^{2+}

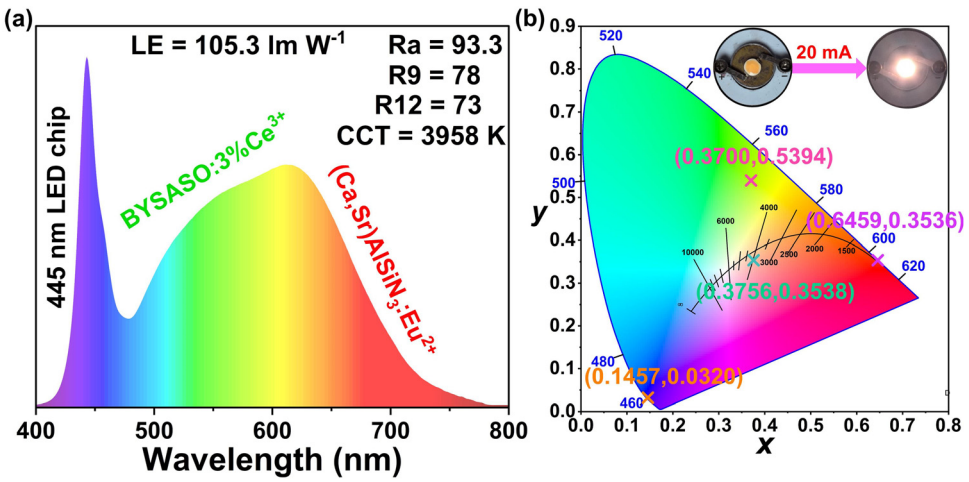

Fig. 5 (a) EL spectra of the white LED device under a 20-mA driving current. (b) CIE chromaticity coordinates of the as-fabricated white LED device. Insets show the digital photographs of the corresponding device with and without a driving current of 20 mA.

Table 4 Optical performances of the fabricated LED device under different driving currents

Current (mA)	R_a	CCT (K)	CIE (x, y)	LE (lm W^{-1})
20	93.3	3958	(0.3756, 0.3538)	105.3
40	93.3	3959	(0.3756, 0.3537)	103.3
60	92.5	3944	(0.3763, 0.3549)	99.1
80	92.3	3936	(0.3767, 0.3555)	96.1
100	92.5	3945	(0.3762, 0.3547)	95.6
200	91.5	3957	(0.3752, 0.3523)	76.8
300	91.6	3962	(0.3742, 0.3493)	48.9

red phosphor (0.6459, 0.3536), the corresponding color coordinates of this device in Fig. 5b are evaluated as (0.3756, 0.3538), which are located within the warm white light region. The chromaticity parameters under the different driving currents are presented in Table 4. Impressively, all R_a parameters are greater than 90 and the CCT values remain around 3950 K. Additionally, the corresponding chromaticity shift under varying current from 20 mA to 300 mA can be calculated as 2.97×10^{-3} using eqn (11) above, indicating that this newly prepared white LED device is stable and reliable under different currents. The successfully prepared white LED has exceptional optical properties, such as high CRI, low CCT value, as well as a small chromaticity shift, indicating that the blue-excited broadband BYSASO:Ce^{3+} green-emitting garnet phosphor synthesized in this study are promising candidates as green-fluorescent materials for high-quality solid-state lighting.

4. Conclusion

The discovery of a novel BYSASO garnet phase has provided a new substrate for cerium-activated phosphors. The relationship between the structure, composition, and PL properties of a series of concentration-dependent BYSASO:xCe^{3+} (x = 0.5–7%) phosphors prepared by a conventional solid-phase reaction method has been investigated in detail *via* the examination of the coordination environment around the active site polyhedron with respect to the optical properties. The crystal structure of the selected example, BYSASO:3%Ce^{3+}, crystallized in the cubic garnet crystal system with the $Ia\bar{3}d$ space group ($a = b = c$ = 12.31961 Å, $\alpha = \beta = \gamma = 90^\circ$ and V = 1869.780(0.034) Å^3). When excited by blue light at 439 nm, the optimal BYSASO:3%Ce^{3+} sample features a bright green emission peak at about 532 nm with an impressive FWHM of up to 125 nm, along with a satisfactory IQE of 80.1% and suitable CIE color coordinates of (0.3700, 0.5394). The investigation of thermal quenching behavior indicates that it can maintain 73.9% luminescence emission intensity at 423 K compared to room temperature. Finally, a high-performance white LED device with a desired R_a of 93.3 and low CCT of 3958 K, as well as an excellent LE value of 105.3 lm W^{-1} is fabricated by coupling the BYSASO:3%Ce^{3+} green phosphor and the commercial (Ca,Sr)AlSiN$_3$:Eu^{2+} red phosphor upon a 445 nm blue LED chip. The findings suggest that this novel BYSASO:Ce^{3+} green phosphor can potentially serve as a conversion material for high-quality solid-state lighting.

Author contributions

Xiaoyuan Chen: investigation; data curation; writing – original draft. Xiaoyong Huang: conceptualization; investigation; supervision; funding acquisition; resources; writing – review & editing.

Data availability

Data are available on request from the authors.

Conflicts of interest

There are no conflicts to declare.

Acknowledgements

This work was supported by the Fundamental Research Program of Shanxi Province (No. 20210302123153), and the Young Sanjin Scholars Distinguished Professor Program of Shanxi Province.

References

1 M.-H. Fang, Z. Bao, W.-T. Huang and R.-S. Liu, *Chem. Rev.*, 2022, **122**, 11474–11513.
2 X. Huang, S. Han, W. Huang and X. Liu, *Chem. Soc. Rev.*, 2013, **42**, 173–201.
3 S. Pimputkar, J. S. Speck, S. P. DenBaars and S. Nakamura, *Nat. Photonics*, 2009, **3**, 180–182.
4 Y. Liu, M. S. Molokeev and Z. Xia, *Energy Mater. Adv.*, 2021, **2021**, 2585274.
5 X. Gao, F. Wu, Y. Zeng, K. Chen, X. Liu and L. Zhu, *J. Mater. Chem. C*, 2023, **11**, 11218–11224.
6 T. Wang, D. Zhou, Z. Yu, T. Zhou, R. Sun, Y. Wang, X. Sun, Y. Wang, Y. Shao and H. Song, *Energy Mater. Adv.*, 2023, **4**, 0024.
7 Z. Zhao, S. Chu, J. Lv, Q. Chen, Z. Xiao, S. Lu and Z. Kan, *J. Mater. Chem. C*, 2023, **11**, 11167–11174.
8 J. Dou and Q. Chen, *Energy Mater. Adv.*, 2022, **2022**, 0002.
9 J. Du, R. Zhu, L. Cao, X. Li, X. Du, H. Lin, C. Zheng and S. Tao, *J. Mater. Chem. C*, 2023, **11**, 11147–11156.
10 S. Hariyani, M. Sójka, A. Setlur and J. Brgoch, *Nat. Rev. Mater.*, 2023, **8**, 759–775.
11 K. Panigrahi and A. Nag, *J. Phys. Chem. C*, 2022, **126**, 8553–8564.
12 Y. Zhuo and J. Brgoch, *J. Phys. Chem. Lett.*, 2021, **12**, 764–772.
13 E. F. Schubert and J. K. Kim, *Science*, 2005, **308**, 1274–1278.
14 G. Blasse and A. Bril, *Appl. Phys. Lett.*, 1967, **11**, 53–55.
15 X. Huang, *Nat. Photonics*, 2014, **8**, 748–749.
16 X. Huang, *Sci. Bull.*, 2019, **64**, 1649–1651.
17 S. Wang, Q. Sun, B. Devakumar, J. Liang, L. Sun and X. Huang, *RSC Adv.*, 2019, **9**, 3429–3435.
18 X. Huang, J. Liang, S. Rtimi, B. Devakumar and Z. Zhang, *Chem. Eng. J.*, 2021, **405**, 126950.

19 X. Huang, Z. Xu and B. Devakumar, *Ceram. Int.*, 2023, **49**, 26420–26427.
20 S. Wang, B. Devakumar, Q. Sun, J. Liang, L. Sun and X. Huang, *J. Mater. Chem. C*, 2020, **8**, 4408–4420.
21 N. Ma, W. Li, B. Devakumar and X. Huang, *Inorg. Chem.*, 2022, **61**, 6898–6909.
22 X. Huang, Q. Sun and B. Devakumar, *Mater. Today Chem.*, 2020, **17**, 100288.
23 G. Li, Y. Tian, Y. Zhao and J. Lin, *Chem. Soc. Rev.*, 2015, **44**, 8688–8713.
24 S. Huang, M. Shang, Y. Yan, Y. Wang, P. Dang and J. Lin, *Laser Photonics Rev.*, 2022, **16**, 2200473.
25 J. Liang, B. Devakumar, L. Sun, S. Wang, Q. Sun and X. Huang, *J. Mater. Chem. C*, 2020, **8**, 4934–4943.
26 J. Zhong, Y. Zhuo, S. Hariyani, W. Zhao, J. Wen and J. Brgoch, *Chem. Mater.*, 2019, **32**, 882–888.
27 N. Hirosaki, R.-J. Xie, K. Kimoto, T. Sekiguchi, Y. Yamamoto, T. Suehiro and M. Mitomo, *Appl. Phys. Lett.*, 2005, **86**, 211905.
28 K. A. Denault, J. Brgoch, M. W. Gaultois, A. Mikhailovsky, R. Petry, H. Winkler, S. P. DenBaars and R. Seshadri, *Chem. Mater.*, 2014, **26**, 2275–2282.
29 S. Wang, Z. Song and Q. Liu, *J. Mater. Chem. C*, 2023, **11**, 48–96.
30 Z. Xia and A. Meijerink, *Chem. Soc. Rev.*, 2017, **46**, 275–299.
31 Y. Qiang, Y. Liu, J. Chen, S. Liu, L. Zhang, H. Kang, F. Xu, Z. Xiao, W. You, L. Han and X. Ye, *J. Lumin.*, 2020, **224**, 117293.
32 J. Liang, L. Sun, S. Wang, Q. Sun, B. Devakumar and X. Huang, *J. Alloys Compd.*, 2020, **836**, 155469.
33 L. Cao, W. Li, B. Devakumar, N. Ma, X. Huang and A. F. Lee, *ACS Appl. Mater. Interfaces*, 2022, **14**, 5643–5652.
34 Y. H. Kim, H. J. Kim, S. P. Ong, Z. Wang and W. B. Im, *Chem. Mater.*, 2020, **32**, 3097–3108.
35 K. Momma and F. Izumi, *J. Appl. Crystallogr.*, 2011, **44**, 1272–1276.
36 T. Roisnel and J. Rodríguez-Carvajal, *Mater. Sci. Forum*, 2001, **378**, 118–123.
37 R. D. Shannon, *Acta Crystallogr.*, 1976, **A32**, 751–767.
38 C. G. Pope, *J. Chem. Educ.*, 1997, **74**, 129–131.
39 A. M. Pires and M. R. Davolos, *Chem. Mater.*, 2001, **13**, 21–27.
40 J. H. Nobbs, *Rev. Prog. Color*, 1985, **15**, 66–75.
41 C. Li and J. Zhong, *Chem. Mater.*, 2022, **34**, 8418–8426.
42 Z. Liao, M. Sójka, J. Zhong and J. Brgoch, *Chem. Mater.*, 2024, **36**, 4654–4663.
43 X. Chen and X. Huang, *J. Alloys Compd.*, 2024, **997**, 174906.
44 M. Zhao, Q. Zhang and Z. Xia, *Acc. Mater. Res.*, 2020, **1**, 137–145.
45 Y. Xiao, W. Xiao, L. Zhang, Z. Hao, G.-H. Pan, Y. Yang, X. Zhang and J. Zhang, *J. Mater. Chem. C*, 2018, **6**, 12159–12163.
46 Y. Wang, J. Ding and Y. Wang, *J. Phys. Chem. C*, 2017, **121**, 27018–27028.
47 V. Bachmann, C. Ronda and A. Meijerink, *Chem. Mater.*, 2009, **21**, 2077–2084.
48 A. L. Companion and M. A. Komarynsky, *J. Chem. Educ.*, 1964, **41**, 257–262.
49 L. Jiang, X. Jiang, Y. Zhang, C. Wang, P. Liu, G. Lv and Y. Su, *ACS Appl. Mater. Interfaces*, 2022, **14**, 15426–15436.
50 M. Liang, J. Xu, Y. Qiang, H. Kang, L. Zhang, J. Chen, C. Liu, X. Luo, Y. Li, J. Zhang, L. Ouyang, W. You and X. Ye, *J. Rare Earths*, 2021, **39**, 1031–1039.
51 F. C. Palilla, A. K. Levine and M. R. Tomkus, *J. Electrochem. Soc.*, 1968, **115**, 642–644.
52 Y. Q. Li, G. de With and H. T. Hintzen, *J. Alloys Compd.*, 2004, **385**, 1–11.
53 D. L. Dexter and J. H. Schulman, *J. Chem. Phys.*, 1954, **22**, 1063–1070.
54 G. Blasee, *J. Solid State Chem.*, 1986, **62**, 207–211.
55 L. G. V. Uitert, *J. Electrochem. Soc.*, 1967, **114**, 1048–1053.
56 X. Chen and X. Huang, *Inorg. Chem.*, 2024, **63**, 5743–5752.
57 M. Iwaki, K. Uematsu, M. Sato and K. Toda, *Inorg. Chem.*, 2023, **62**, 1250–1256.
58 Y. Wang, J. Ding, X. Zhou and Y. Wang, *Chem. Eng. J.*, 2020, **381**, 122528.
59 Y.-C. Lin, M. Bettinelli and M. Karlsson, *Chem. Mater.*, 2019, **31**, 3851–3862.
60 Y. H. Kim, P. Arunkumar, B. Y. Kim, S. Unithrattil, E. Kim, S.-H. Moon, J. Y. Hyun, K. H. Kim, D. Lee, J.-S. Lee and W. B. Im, *Nat. Mater.*, 2017, **16**, 543–550.
61 M. Amachraa, Z. Wang, C. Chen, S. Hariyani, H. Tang, J. Brgoch and S. P. Ong, *Chem. Mater.*, 2020, **32**, 6256–6265.
62 J. Zhong, W. Zhuang, X. Xing, R. Liu, Y. Li, Y. Liu and Y. Hu, *J. Phys. Chem. C*, 2015, **119**, 5562–5569.
63 J. Chan, L. Cao, W. Li, N. Ma, Z. Xu and X. Huang, *Inorg. Chem.*, 2022, **61**, 6953–6963.
64 Y.-C. Lin, M. Bettinelli, S. K. Sharma, B. Redlich, A. Speghini and M. Karlsson, *J. Mater. Chem. C*, 2020, **8**, 14015–14027.
65 K. J. Laidler, *J. Chem. Educ.*, 1984, **61**, 494–498.
66 L. Huang, Y. Liu, J. Yu, Y. Zhu, F. Pan, T. Xuan, M. G. Brik, C. Wang and J. Wang, *ACS Appl. Mater. Interfaces*, 2018, **10**, 18082–18092.
67 L. Huang, Y. Zhu, X. Zhang, R. Zou, F. Pan, J. Wang and M. Wu, *Chem. Mater.*, 2016, **28**, 1495–1502.
68 Y. Chen, F. Pan, M. Wang, X. Zhang, J. Wang, M. Wu and C. Wang, *J. Mater. Chem. C*, 2016, **4**, 2367–2373.

